

RESEARCH

Open Access



Tensile Test and Numerical Simulation Investigations on the Mechanical Properties of a New Type of Slightly Curved Arc HRB400 Steel Bars in Mass Concrete

Li Gao^{1,2}, Mei-Ling Zhuang^{3,4*}, Fangzhi Zhu^{1,2}, Chuanzhi Sun^{1,2} and Jun Yang⁵

Abstract

The temperature stress in mass concrete structure is relatively high during construction, which usually leads to temperature cracks. To solve this problem, concrete blocks are usually placed by setting wide slots. Connecting the truncated steel bars at the position of the wide slots by welding or extruding sleeves has many disadvantages. To solve the problem of temperature-induced stress loss, a new type of slightly curved arc HRB400 (SCAHRB400) steel bars was proposed without cutting off the steel bars in this article. Tensile tests and numerical simulations were performed for five types of SCAHRB400 steel bars considering geometric and material nonlinearity. Based on the test results and numerical simulation results, the equivalent stress–strain relationships of SCAHRB400 steel bars were established, and the emergence of the plastic zone of SCAHRB400 steel bars in the tensile process were observed, the tensile properties of SCAHRB400 steel bars were analyzed and discussed. The test results indicate that SCAHRB400 steel bars are prone to local yielding near the crown of large arches and at the connection of horizontal and arc sections. The numerical simulation equivalent stress–strain curves have good regularity. The equivalent stress–strain curves of slightly curved arc HRB400 and HRB335 steel bars have the similar changing law. When the stress is small, the tensile stiffness and compressive axial stiffness of slightly curved arc HRB400 and HRB335 steel bars are similar; when the stress is large, the axial stiffness of SCAHRB400 steel bars is greater than that of slight curved arc HRB335 steel bars. Through test and numerical simulation studies, the theoretical basis can be established for the engineering application of new slightly curved arc steel bars in mass concrete.

Keywords Mass concrete, Temperature cracks, Slightly curved arc steel bar, Mean stress–strain relationship, Plastic zone

Journal information: ISSN 1976-0485 / eISSN 2234-1315

*Correspondence:

Mei-Ling Zhuang

ml_zhuang99@163.com

Full list of author information is available at the end of the article



© The Author(s) 2023. **Open Access** This article is licensed under a Creative Commons Attribution 4.0 International License, which permits use, sharing, adaptation, distribution and reproduction in any medium or format, as long as you give appropriate credit to the original author(s) and the source, provide a link to the Creative Commons licence, and indicate if changes were made. The images or other third party material in this article are included in the article's Creative Commons licence, unless indicated otherwise in a credit line to the material. If material is not included in the article's Creative Commons licence and your intended use is not permitted by statutory regulation or exceeds the permitted use, you will need to obtain permission directly from the copyright holder. To view a copy of this licence, visit <http://creativecommons.org/licenses/by/4.0/>.

1 Introduction

Mass concrete structures are common in hydraulic and hydropower projects. During construction, the temperature stresses in mass concrete are relatively large. At the same time, the mass concrete structure is prone to large temperature stresses influenced by the external ambient temperature (Lu et al., 2021; Yang et al., 2019), leading to thermal cracks in concrete structures (Xin et al., 2021). Therefore, wide slots are set to cast the mass concrete into blocks, and the wide slots are backfilled to form a whole in the later low-temperature season. This measure has proven to be effective in reducing and avoiding temperature cracks. It is often used in engineering (Li et al., 2017).

There are usually stressed steel bars passing through the wide grooves. As the heat of hydration of the concrete decreases, the concrete and the straight steel bars on both sides of the wide slot shrink. Due to the confining effect (Chen & Zhang, 2014; Woo et al., 2018), the steel bar generates large tensile stresses during construction (Liu et al., 2010), which reduces the load-bearing of steel bars during the construction period (Jiang et al., 2007). Lateral concrete also produces tensile stress and is more prone to cracking during construction (Gao & Fang, 2013; Yan et al., 2013). It is common practice to cut the steel bar across the wide slot within 24 to 48 h after the concrete is poured on both sides of the wide slot, and then connect it as a whole when the wide slot is backfilled later in the cold season. Typically, extruded sleeve connections and welded connections are used to connect the steel bars. Currently, there are three ways to pass the steel bar through the wide slot, such as no cutting the steel bar, extruded sleeve connection after cutting the steel bar, and welded connection after cutting the steel bar (Shi & Hou, 2013). However, it is difficult to operate the way of the steel bar across the wide slot using pre-cut and post-connected. It is almost impossible and costly to implement when there are many layers of reinforcement crossing wide slots. Therefore, the treatment of steel bar across wide slot is a pressing challenge in construction. Fig. 1 shows the slightly curved arc steel bars (SCASB) across wide slot (Ma, 2014). The steel bar is not cut off. The SCASB across wide slot is used to accommodate the temperature deformation of the concrete on both sides of the wide slot by using the expansion and contraction of its slightly curved arc section. Due to the existence of the slightly curved arc section, its axial stiffness is less than that of the straight reinforcement, thus reducing the restriction on the temperature deformation of the concrete on both sides of the wide slot, but in the slightly curved arc section, stress concentration occur at the top of the arc and at the backbend point of the SCASB, and these parts tend to enter the plastic state.

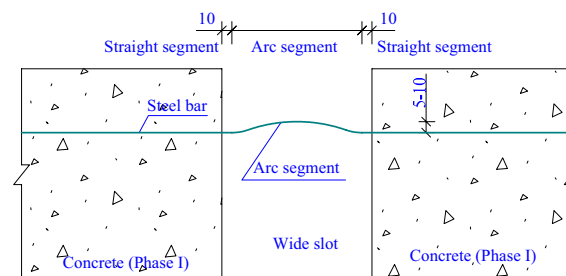


Fig. 1 Arc-shaped crotch wide groove steel bar (unit: cm)

Suitable SCASB do not exhibit plasticity in their any part during construction. They can effectively reduce the temperature stresses in themselves and in the concrete on both sides of the wide slot. Due to the temperature effect and the huge size of the mass concrete to be considered, the appropriate shape and size of the SCASB can only be determined by numerical calculations. In practical engineering, the SCASB are placed horizontally in an arc and laid flat in a wide slot, so structures or members reinforced with SCASB should be calculated as a spatial problem and the beam element should be used to simulate the SCASB. The axial stiffness of SCASB is small and its deformation is large, so it should take into account the geometric nonlinearity. When the slightly curved arc section has part of plasticity, it also needs to consider the material nonlinearity. If the equivalent stress–strain relationship can be obtained from the material properties tests and numerical simulations of SCASB, where the stress is taken as the ratio of the axial force to the cross-sectional area of the steel bar, i.e., the average stress, and the strain is taken as the average strain calculated using the width of the wide slot as the scale distance, as well as the average stress level in the plastic zone, the SCASB can be converted into a straight steel bar for calculation, and the space problem can be converted to a plane problem.

In this article, five types of slightly curved arc HRB400 (SCAHRB400) steel bars were investigated through tensile tests. Considering the geometric nonlinearity and material nonlinearity, finite element models of slightly curved arc HRB400 steel bars were established to simulate their tension and compression stresses. The numerical simulation equivalent stress–strain curves of SCAHRB400 steel bars have good regularity. The numerical simulation results are not very different from the test results, indicating that the numerical simulation curves are reliable. According to the test and numerical simulation results, the equivalent stress–strain relationship of five types of SCAHRB400 steel bars was established, the plastic zone appearance process of SCAHRB400 steel bars in the tension–compression process was analyzed,

and the mechanical properties of SCAHRB400 steel bars under tension and compression stresses were obtained.

2 Tensile Test and Results

2.1 Design and Fabrication of SCAHRB400 Steel Bar Specimens

During construction, the larger arch height the SCASB across wide slot in mass concrete was, the smaller stress caused by concrete expansion or contraction was. However, during normal operation, the stretching of SCASB in the curved arc section produced a tensile stress perpendicular to the direction of the steel bar, making the concrete appear to be cracked along the steel bar. When

the arch height of the curved arc section was larger, the tensile stress perpendicular to the direction of the steel bar, the concrete tended to appear cracks along the direction of the steel bar. The design basis was mainly based on the different width of the wide slot.

The design details of the five types of SCAHRB400 steel bars across a wide slot are shown in Fig. 2. Among them, the first four forms were the same, 1 big arc + 2 small arc + 2 horizontal sections, the length of each horizontal section was 100 mm, and the radiuses of the arcs were different. The wide slot widths of the first three types of SCAHRB400 steel bars were 1.5 m, and that of the fourth type of SCAHRB400 steel bars was 1.2 m. The fifth type

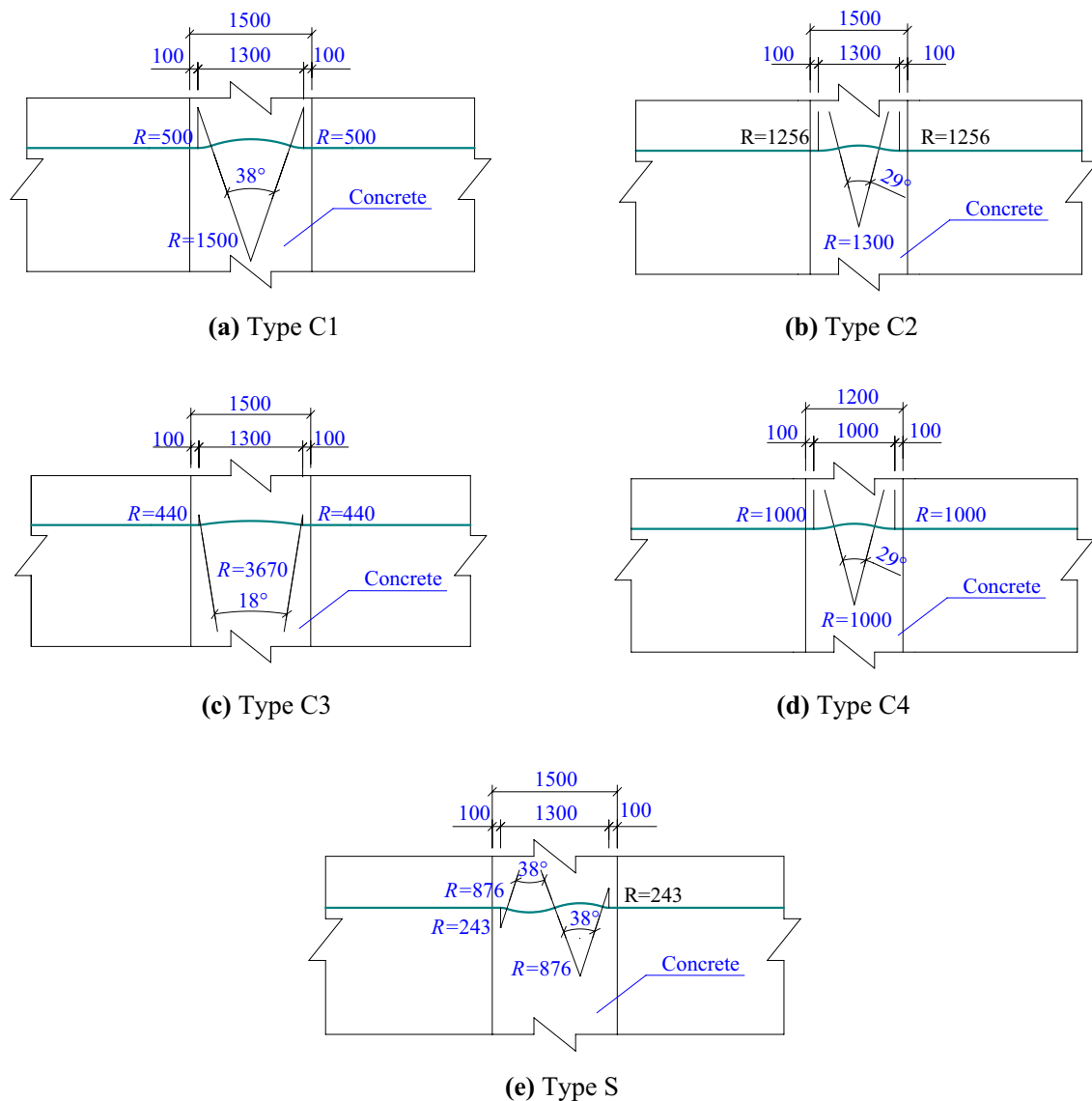


Fig. 2 Shapes and dimensions of the SCAHRB400 steel bars

of the steel bars consists of 2 large arcs + 2 small arcs + 2 horizontal sections, forming an S-shape. The length of each horizontal section was also 100 mm. The wide slot width of it was 1.5 m.

Tensile tests were carried out on three specimens of each type of SCAHRB400 steel bars. The measured dimensional parameters of each specimen are shown in Table 1. In this article, the test specimens were made by conventional steel bending machines, and there were inevitable errors in the dimensional control of the specimens. The test specimens with diameters of 36 mm are shown in Fig. 3. The measured modulus of elasticity of the steel bars was 2×10^5 MPa. In tensile tests, the non-linearity of the material is mainly reflected in the stress–strain curve of the SCAHRB400 steel bar specimens. It is well known that reinforcing steel is an obvious nonlinear material with four distinct phases of unidirectional tensile properties, namely, elastic deformation phase, yield phase, strengthening phase, and necking phase. SCAHRB400 steel bars did not vary uniformly in cross-sectional plasticity during the tensile process due to their specific shape.

2.2 Loading and Measurement

The loading mechanism was specially designed for the axial tensile test, as shown in Fig. 4a, and the photograph of the test device is shown in Fig. 4b. Both ends of the SCAHRB400 steel bars were threaded. The steel bar was fixed by means of a nut. The tensioning of the bar was achieved by twisting the nut. The displacement of the measuring point of the steel bar was measured with a percentage meter. To prevent the slightly curved steel bar

from rotating during loading, an anti-rotation limit plate was provided at the loading end.

To obtain the equivalent stress–strain curve for a SCAHRB400 steel bar within a wide slot width ($l_0 + 2l_2$), the strain was the average strain calculated using the wide slot width as the scale distance, and the stress was the ratio of the axial force to the cross-section of the steel bar (average stress), so the displacement measurement points should ideally be located at a distance ($l_0 + 2l_2$) from the wide slot width (see Fig. 5). However, the test was set up to avoid torsional deformation of the specimen during loading, which affects the installation of the percentage meter, the displacement measurement points can only be arranged at the two ends of the slightly curved arc section of the steel bar, and the distance between the two points was l_0 . To obtain the average strain of the SCAHRB400 steel bar across the wide slot, the strain gauges A and B (see Fig. 5) were arranged near the ends of the slightly curved arc section of the steel bar, which were located on the upper surface of the steel bar. In this way, the average strain over the length of the wide slot width ($l_0 + 2l_2$) can be calculated from Eq. (1):

$$\varepsilon = \frac{(\varepsilon_A + \varepsilon_B)l_2 + \Delta}{l_0 + 2l_2}, \quad (1)$$

where Δ was the elongation over the length of l_0 ; ε_A and ε_B were the strains at points A and B; and l_0 and l_2 are shown in Fig. 5.

2.3 Test Results

The equivalent stress–strain curve is plotted in Fig. 6. The stresses of the three C-shaped SCAHRB400 steel

Table 1 Dimension parameters of SCAHRB400 steel bar specimens

Types	Design vector span height (mm)	Measured vector span height (mm)	Design vector span length (mm)	Measured vector span length (mm)	Specimen no.
36C1	109.0	105	1300	1292	Test-36C1-a;
		103		1293	Test-36C1-b;
		107		1295	Test-36C1-c
36C2	83.0	77	1300	1290	Test-36C2-a;
		77		1294	Test-36C2-b;
		77		1296	Test-36C2-c
36C3	51.5	55	1300	1295	Test-36C3-a;
		51		1296	Test-36C3-b;
		51		1302	Test-36C3-c
36C4	63.5	59	1000	985	Test-36C4-a;
		60		989	Test-36C4-b;
		61		990	Test-36C4-c
36S	54.0	(54 + 55)	1300	1295	Test-36S-a;
		(50 + 53)		1296	Test-36S-b;
		(50 + 50)		1301	Test-36S-c



(a) 36C1



(b) 36C2



(c) 36C1

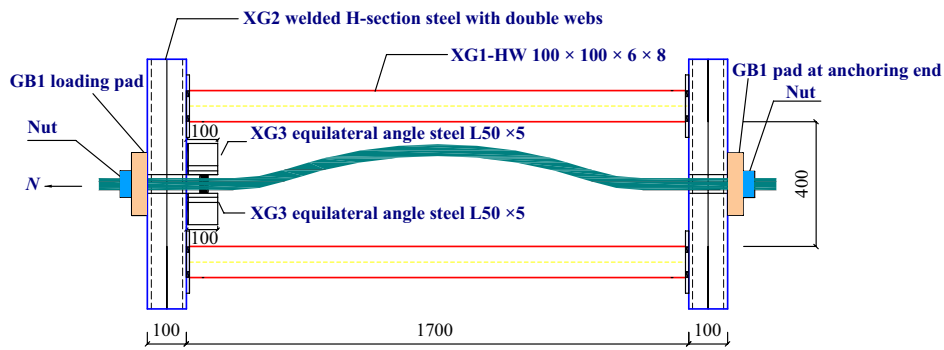


(d) 36C2



(e) 36S

Fig. 3 Photos of the specimens



(a) Design of loading mechanism



(b) Photo of the test device

Fig. 4 Test device

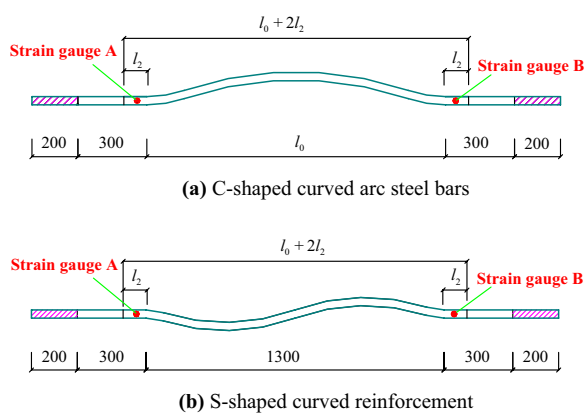


Fig. 5 Spacing and strain gauge patch location

bar specimens do not differ much. The stresses of the three S-shaped SCAHRB400 steel bar specimens fluctuate slightly more than those of the C-shaped specimens because of the relatively large difference in the size of the members. The left end of the specimen is fixed and its right end is in tension. The tensioning end is twisted by screwing. The tensioning device is equipped with a torsion-limiting mechanism, but the tensioning end still produces a small turning angle. Torque in the process of transferring to the fixed end, the torsional stiffness of the curved section is small. Most of the torsional deformation occurs in the curved section. The torsional effect of the fixed end A is not obvious. As a result, the strain at point B is slightly more affected by

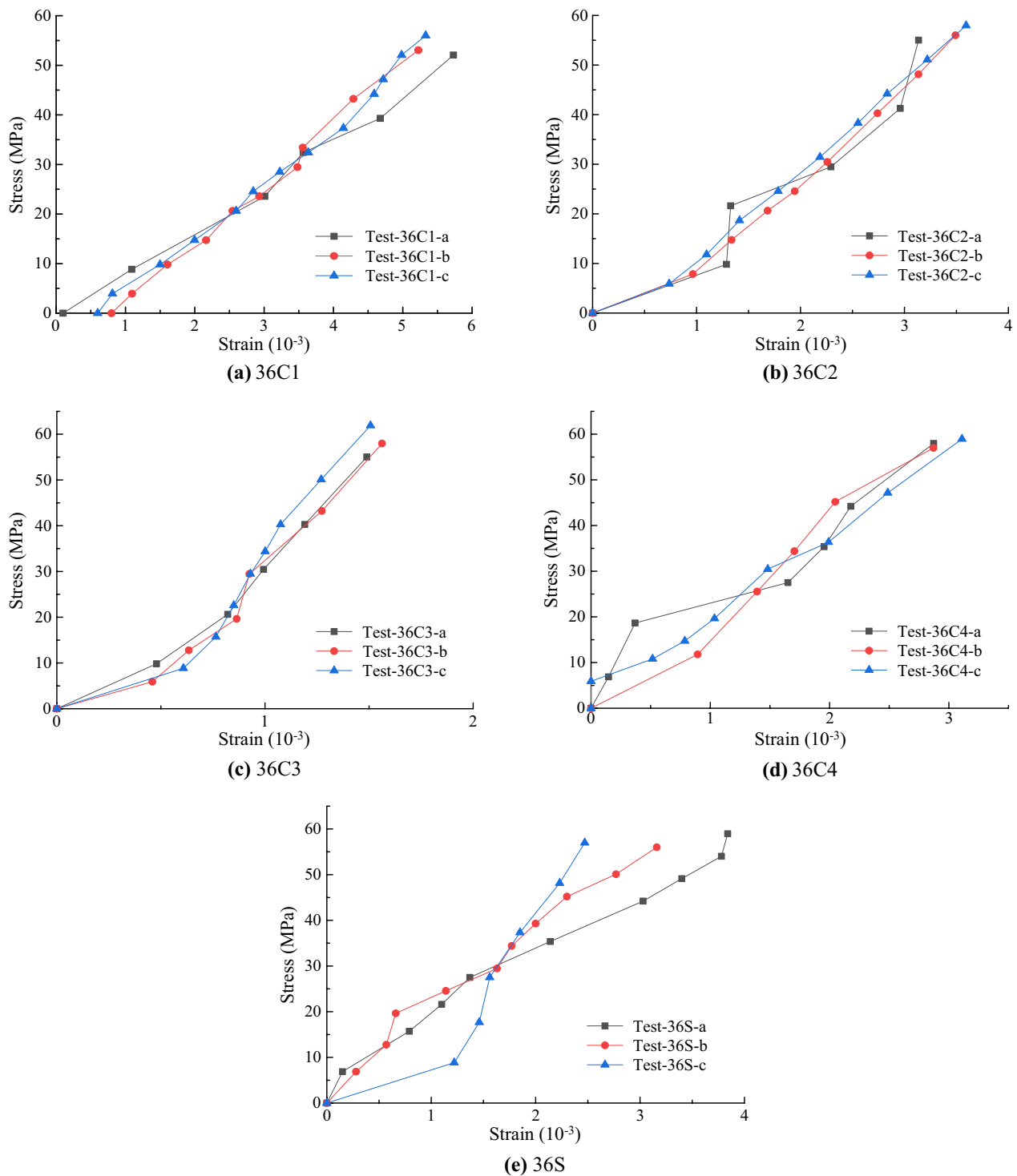


Fig. 6 Equivalent stress–strain curves of specimens

torsional tension than that at point A. The equivalent stress–strain curves of C-shaped specimens are linear as a whole. The equivalent stress–strain curves of S-shaped specimens change greatly because there are

errors in the fabrication of S-shaped specimens, and the S-shaped structure makes the plastic deformation zone of the steel bar section unstable, which is also reflected in the later numerical calculation.

Comparison of test results of the five types of specimens is summarized in Fig. 7. For C-type specimens 36C1–36C4, the stress corresponding to the same strain increases with the decrease of the vector span height. It indicates that the deformation of 36C3 specimens is the smallest under the influence of the temperature stress of concrete on both sides of the wide slot. The vector span length has little effect on the equivalent stress–strain curve of the specimens. The equivalent stress–strain curves of 36S-shaped specimens are more complex because of the S-shaped height characteristics. It indicates that the equivalent stress–strain curves of SCAHRB400 steel bar specimens are not only related to the vector span height, but also related to the shape of the arc. The selection of the shape and vector span height of SCAHRB400 steel bar specimens should be combined with the position of the wide slot on the site.

3 Numerical Simulation Results

3.1 Finite Element Models

Considering the geometric nonlinearity and material nonlinearity, ANSYS software was used to simulate the equivalent stress–strain curve of the SCAHRB400 steel bars, as shown in Fig. 2. As the stresses in the SCAHRB400 steel bars did not exceed 100 MPa before the wide slot was backfilled, each specimen was calculated to end when its average stress reached 100 MPa. The material stress–strain curves were performed using the ideal elasti-plastic model BISO, where the yield strength f_y of the steel bars was taken as 415 MPa.

According to the symmetry, 1/4 of the structure of specimens 36C1–36C4 was taken for modeling. The finite element model was established using Solid 95 element, which was a 20-node isoparametric element with the ability to consider plasticity, large deformation and

large strain. When the external load increased to a certain level, the outer surface of the steel bar started to yield. As the external load increased, the plastic region becomes larger, the horizontal stiffness of the steel bar decreased. The stress–strain curve obtained using Solid 95 element deviated from that obtained using the beam element and was concave toward the strain axis. This was due to the fact that the Solid 95 element took into account the stiffness drop caused by material nonlinearity, while the beam element did not. Thus, it was more practical to simulate the tensile properties of the SCAHRB400 HRB400 steel bars using Solid 95 element. The sketch and meshing diagram of the finite element model of specimen 36C1 is shown in Fig. 8.

The longitudinal direction along the straight section of the specimen was x -axis, the vertical direction was z -axis and the horizontal direction was y -axis. The x -axis symmetry plane (section 5) imposed x -directional constraints on all nodes, the y -axis symmetry plane imposed normal constraints on all nodes. Straight line section 1–2 was embedded in concrete, and its lower surface nodes (the nodes with the smallest z -axis coordinate values) were vertically constrained. For specimen 36C1, its arc section 3–4 was divided into 16-layer mesh, its arc section 4–5 was divided into 30-layer mesh and the straight line section 1–3 was divided into 50-layer mesh, with 24 elements in each section. For specimen 36C2, its arc section 3–4 was divided into 20-layer mesh, its arc section 4–5 was divided into 20-layer mesh and its straight line section 1–3 was divided into 50-layer mesh, with 24 elements in each section. For specimens 36C3 and 36C4, their arc section 3–4 was divided into 8-layer mesh, their arc section 4–5 was divided into 40-layer mesh and their straight line section 1–3 were divided into 50-layer mesh, with 24 elements in each section.

According to the symmetry, 1/2 of the structure of specimen 36S was taken for modeling. The finite element model was also established using Solid 95 element. The sketch and meshing diagram of specimen 36S is shown in Fig. 9. The longitudinal direction along the straight section of the specimen was x -axis, the vertical direction was z -axis and the horizontal direction was y -axis. Straight line sections 1–2 and 9–10 were embedded in concrete. The lower surface nodes (the nodes with the smallest value in z -axis coordinates) were constrained vertically. The x -directional constraints were imposed on the upper surface nodes of section 6 (the nodes with the largest value in z -axis coordinates), eliminating the horizontal rigid body displacements. Normal constraints were imposed on the y -axis symmetry plane nodes. Horizontal loads were applied to section 1 and section 9 at both ends of the model. Its arc segments 3–4 and 7–8 were divided into a 4-layer mesh, its arc segments 4–6

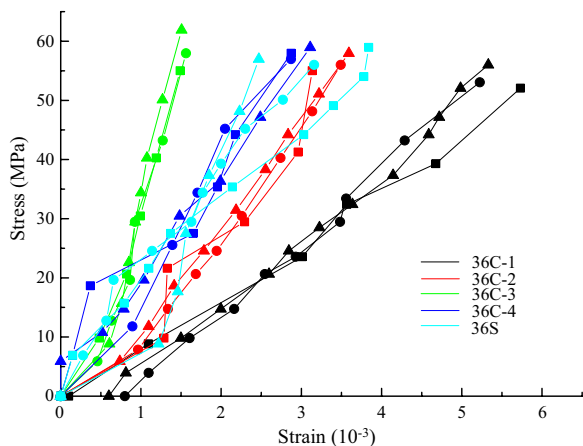


Fig. 7 Comparison of test results of the five types of specimens

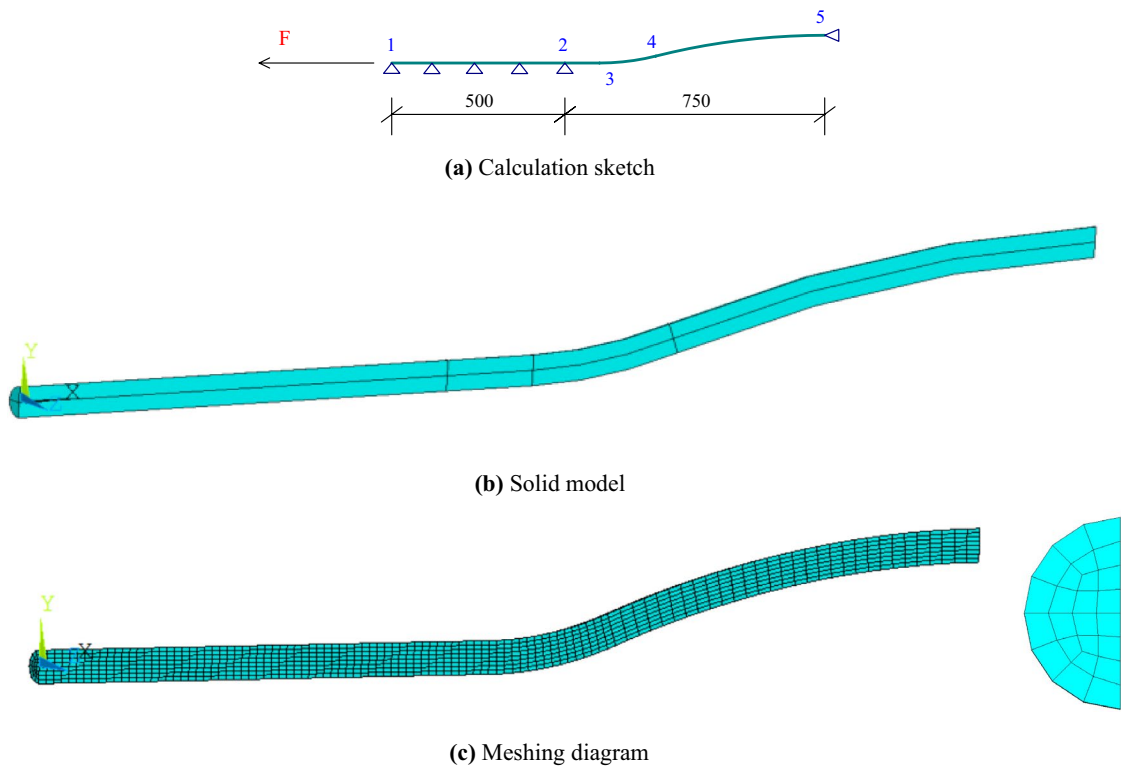


Fig. 8 Calculation and sketch and meshing diagram of specimen 36C1

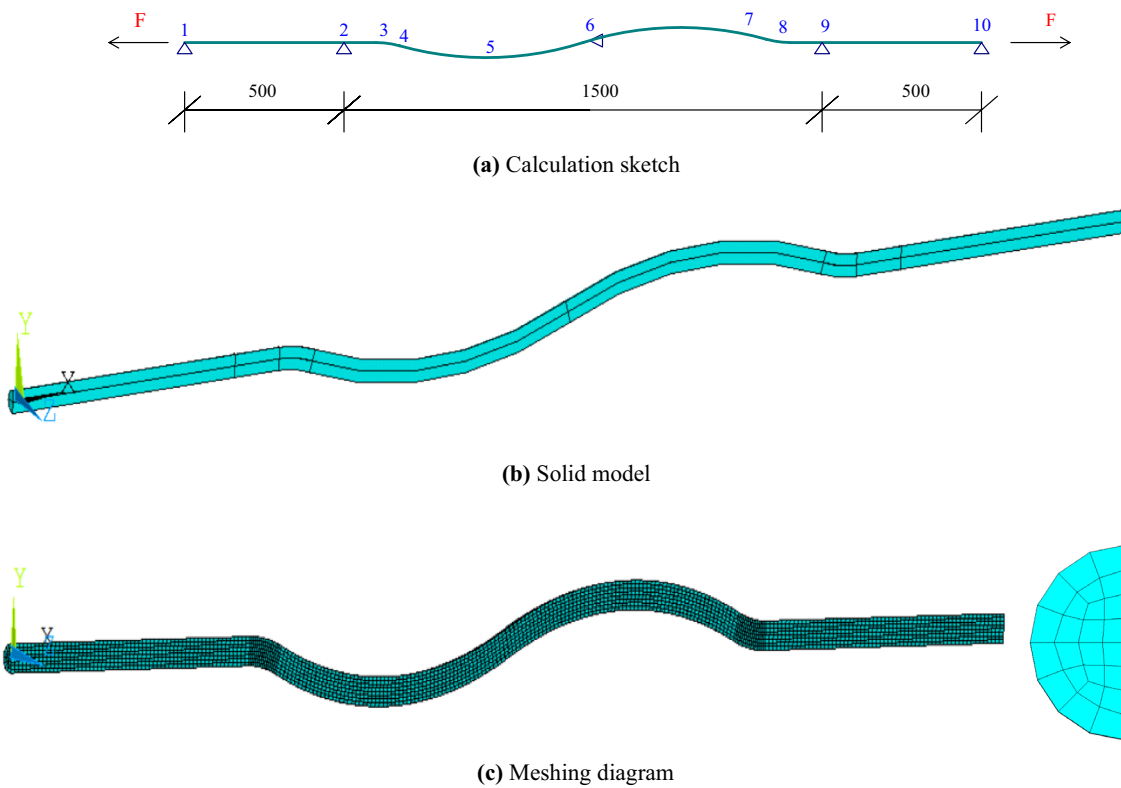


Fig. 9 Calculation sketch and finite element model of specimens 36S

and 6–7 were divided into a 30-layer mesh, and straight line segments 1–3 and 8–10 were divided into a 50-layer mesh, with 24 elements in each section.

3.2 Comparison of Numerical Simulation Results and Test Results

3.2.1 Specimens 36C1–36C4

σ_x stress cloud and deformation diagrams of specimen 36C1 under different loads are given in Figs. 10 and 11. In Fig. 11, the displacement amplification factor is 1 and DMX is the maximum deformation (similar for other operating conditions). The calculated equivalent stress–strain curves for specimens 36C1–36C4 are plotted in Fig. 12, while the equivalent stress–strain curves obtained from the tests are also given.

The axial stiffness of specimen 36C1 decreases as the compressive stress increases. When the external stress $\bar{\sigma} < -35.0$ MPa, its maximum compressive stress does not exceed its yield strength and there is no plastic zone. When $\bar{\sigma} = -35.0$ MPa, its maximum compressive stress exceeds its yield strength, but its plastic zone is small. The calculation results diverge when $\bar{\sigma} = -45.0$ MPa. Under the action of large compressive stress, the possibility of buckling of the steel bar will be elevated and its plastic zone will be increased. The calculation results of nonlinear problems using Finite element analysis software ANSYS are prone to non-convergence, which is a normal phenomenon. It can be calculated to 45 MPa has reached the purpose of the numerical calculation because curved arc steel bars was designed to resist the loss of reinforcement tensile stress brought about by the shrinkage of concrete on both sides of the wide slot, compressive stress is small or does not appear. When the steel bar is in tension and $\bar{\sigma} < 40.0$ MPa, its maximum tensile stress does not exceed its yield strength and there is no plastic zone. When $\bar{\sigma} = 40.0$ MPa, its maximum tensile stress exceeds its yield strength, but its plastic zone is small. When $\bar{\sigma} \leq 50.0$ MPa, the increase in stiffness caused by the straightening of the steel bar and the decrease in vector span height is greater than the decrease in stiffness caused by the increase in the plastic zone of the steel bar, and its axial stiffness increases as its tensile stress increases. When $\bar{\sigma} = 100.0$ MPa, the plasticity in the area around section 5 and section 3 has developed considerably. The plastic zone in section 5 and section 3 exceeds half of the entire section.

The actual vector heights of the three specimens differ somewhat and the stiffness of SCAHRB400 steel bars at the initial tension is small, their displacements are not easily measured accurately, thus the test curves of the three specimens differ somewhat, but they are all in the vicinity of the numerical simulation curves, indicating that the numerical simulation curves are reliable.

The numerical simulation tensile and compressive stress properties of specimens 36C2–36C4 are summarized in Tables 2 and 3. The numerical simulation results of specimens 36C2–36C4 are approximately the same as specimen 36C1. It can be seen from Eq. (1) that the vector span lengths affect the calculation of the average strains. The smaller the measured vector span length is, the larger the average strain is, which leads to the deviation between the experimental data and the numerical simulation results is larger for specimens 36C4 compared with other members.

Fig. 13 gives the numerical simulation stress–strain curves of specimens 36C1–36C4. The axial stiffness of all 36C SCAHRB400 steel bars is much smaller than that of the straight steel bars. The axial stiffness of 36C SCAHRB400 steel bars with the same vector span length decreases as the vector span height increases. As the vector span length of specimen 36C4 is different from the other three, its curve is between those of specimen 36C2 and specimen 36C3. Its equivalent stress–strain curve is only related to vector span height, but it is also affected by the vector span length. The equivalent stress–strain curves of specimens 36C1–36C4 perform the same trend in tension and compression. When the steel bar is compressed, the curve is concave toward the strain axis. When the average tensile stress is small, the curve was concave toward stress axis; the curve is concave toward stress axis with the increase of the average tensile stress. This is because the decrease in the axial stiffness of the steel bar as the compressive stress increases. When the steel bar is in tension, the axial stiffness of the steel bar initially increases with the increase of tensile stress. At this point, the increase in stiffness caused by the straightening of the steel bar and the decrease in vector span height is greater than the decrease in stiffness caused by the increase in the plastic zone of the steel bar. Then, the axial stiffness of the steel bar decreases with the increase of the tensile stress.

3.2.2 Specimen 36S

σ_x stress cloud and deformation diagrams of specimen 36C1 under different loads are given in Figs. 14 and 15, with a displacement amplification factor of 1 in the deformation diagrams. The numerical simulation stress–strain curve of specimen 36S is plotted in Fig. 16, which is compared with the test curves. It can be seen that the stress–strain curves of specimens 36S and 36C1 have the similar changing law. When the steel bar is compressed, the equivalent stress–strain curve is concave toward the strain axis. Its axial stiffness decreases as its compressive stress increases. Its maximum compressive stress exceeds its yield strength when $\bar{\sigma} = -50.0$ MPa. When the steel bar is in tension and $\bar{\sigma} < 45.0$ MPa, its maximum tensile stress

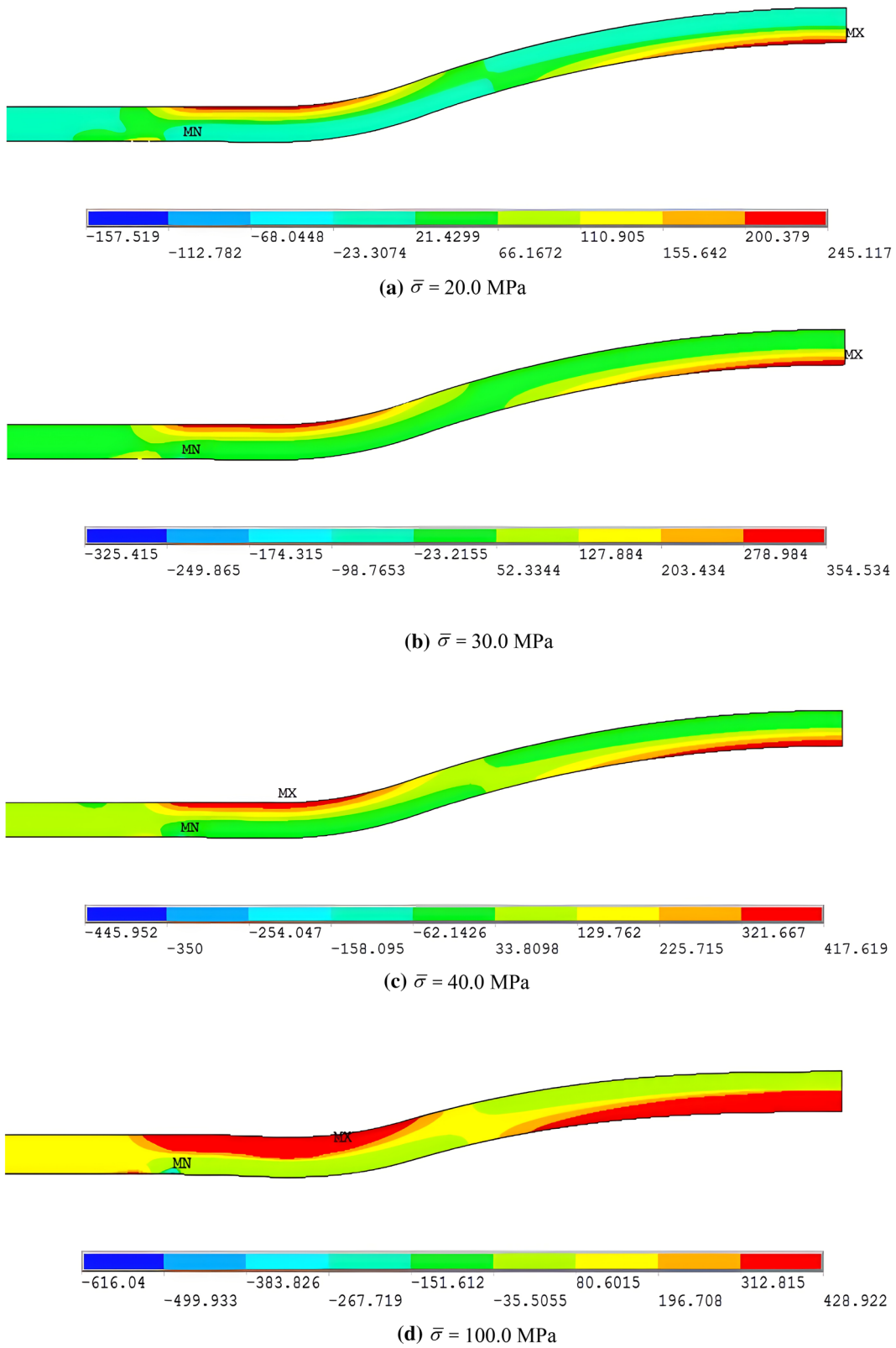


Fig. 10 σ_x stress cloud of specimen 36C1 (unit: MPa)

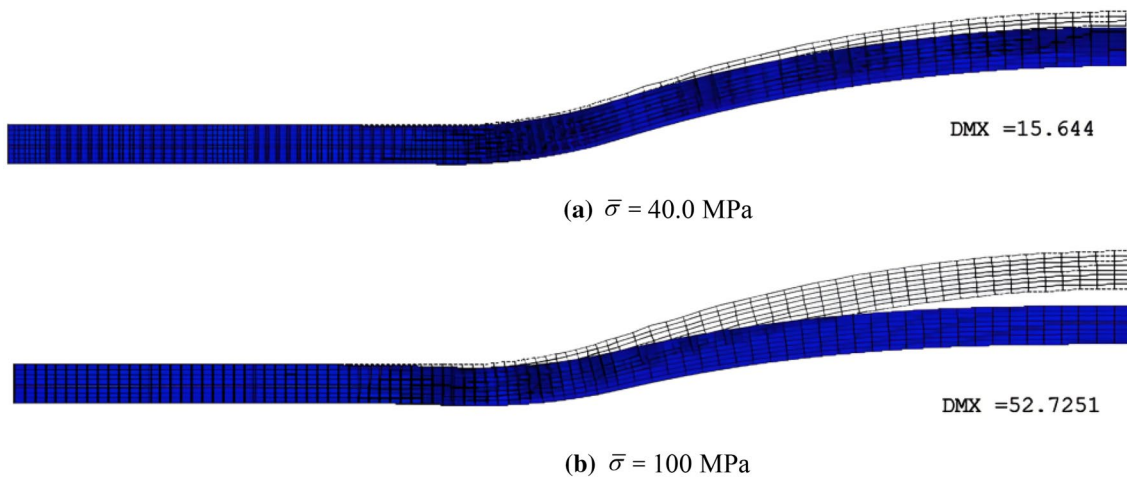


Fig. 11 Deformation diagram of specimen 36C1 (unit: mm)

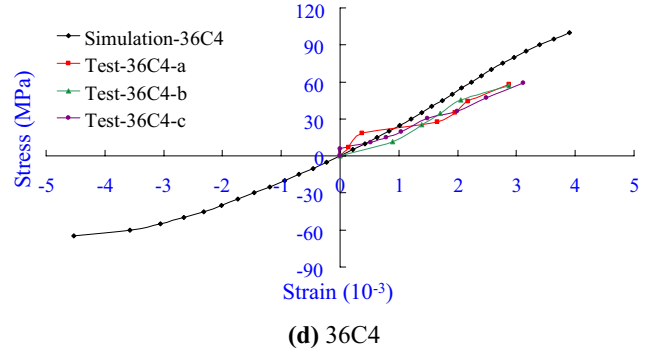
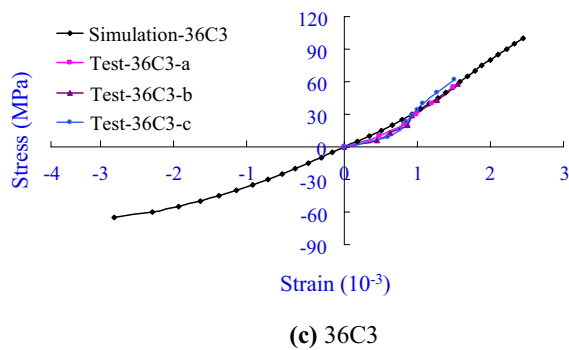
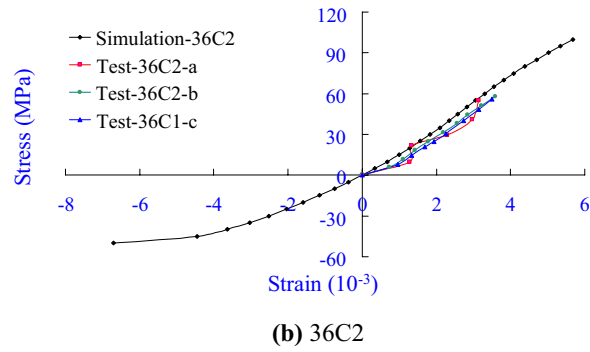
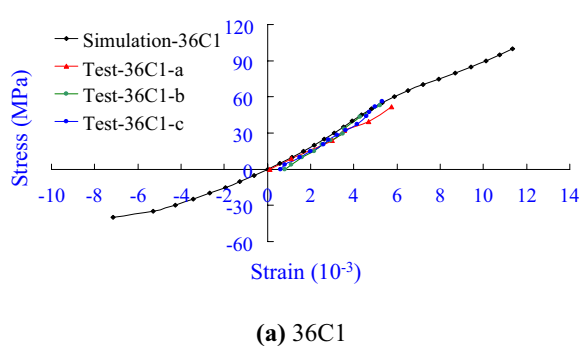


Fig. 12 Comparison of test and numerical simulation equivalent stress–strain curves of specimens 36C1–36C4

do not exceed its yield strength and there is no plastic zone. When $\bar{\sigma} = 45.0$ MPa, its maximum tensile stress exceeds its yield strength, but its plastic zone is small. When $\bar{\sigma} \leq 65.0$ MPa, the curve of the steel bar is concave toward the stress axis. After $\bar{\sigma} > 65.0$ MPa, the curve is concave toward the strain axis. When $\bar{\sigma} = 100.0$ MPa,

the area near the plasticity of section 5 and section 3 has developed considerably and the plastic zone of section 5 is close to 1/2 of the entire section. The test curves of the three specimens are somewhat different, but they are all in the vicinity of the numerical simulation curves.

Table 2 Numerical simulation compressive stress properties of specimens 36C2–36C4

Specimen no.	Stress–strain curves	$\bar{\sigma}$ (MPa)	
		When the maximum compressive stress exceeds the material yield strength	When calculating divergence
36C1	Concave toward strain axis	– 35.0	– 45.0
36C2	Concave toward strain axis	– 40.0	– 55.0
36C3	Concave toward strain axis	– 65.0	– 70.0
36C4	Concave toward strain axis	– 50.0	– 70.0

Table 3 Numerical simulation tensile stress properties of specimens 36C2–36C4

Specimen no.	Stress–strain curves		$\bar{\sigma}$, when the maximum tensile stress exceeds the material yield strength
	Concave toward stress axis	Concave toward strain axis	
36C1	$\bar{\sigma} \leq 50.0$ MPa	$\bar{\sigma} > 50.0$ MPa	40.0
36C2	$\bar{\sigma} \leq 55.0$ MPa	$\bar{\sigma} > 55.0$ MPa	55.0
36C3	$\bar{\sigma} \leq 75.0$ MPa	$\bar{\sigma} > 75.0$ MPa	60.0
36C4	$\bar{\sigma} \leq 65.0$ MPa	$\bar{\sigma} > 65.0$ MPa	50.0

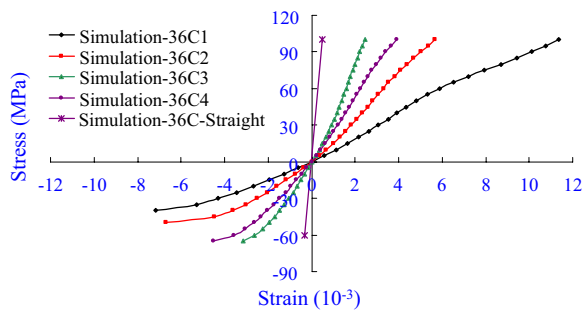


Fig. 13 Numerical simulation stress–strain curves of specimens 36C1 to 36C4

The numerical equivalent stress–strain curves of specimens 36C1–36C4 and 36S are given in Fig. 17. The stress–strain curves of specimens 36C and 36S follow the same trend. When the steel bar is in compression, the equivalent stress–strain curve is concave toward the strain axis. When the steel bar is in tension, the curve is concave toward the stress axis. When the steel bar is in compression, the curve of specimen 36S between the two curves of specimens 36C2 and 36C3, indicating that SCAHRB400 steel bars in compression within the same vector span length has the same changing law. When the steel bar is in tension, the sum of the two arc vector span heights of specimen 36S is the same as the single arc vector span height of specimen 36C1, but its effect is not as good as that of specimen 36C1. The curve of specimen 36S changes basically the

same as that of specimen 36C2, its stress is between those of specimens 36C1 and 36C2 at higher stresses. Combining with the numerical simulation results and test results, it can be concluded that the stress–strain curve of SACHRB400 steel bars at the late stage begun to realize a more obvious nonlinear relationship.

3.3 Comparison of Slightly Curved Arc HRB400 and HRB335 Steel Bars

To understand the difference between the stress–strain curves of HRB400 and HRB335 steel bars, the equivalent stress–strain curves in Yang et al. (2019) and these in this article are presented in Fig. 18. When the steel bar is in compression, the equivalent stress–strain curves are concave toward the strain axis, indicating that the axial stiffness of the steel bar decreases as the compressive stress increases, but the axial stiffness of HRB335 steel bars decreases more rapidly. The compressive stress of the SCAHRB400 steel bars is greater than that of slightly curved arc HRB335 steel bars when the calculation stress is divergent. As the stress increases, both curves change in the same way, concave toward the stress axis, indicating that the axial stiffness of the steel bar increases with the increase in tensile stress, but the stiffness of the SCAHRB400 steel bar increases more quickly. When the stress is greater than a certain value, the curves are concave toward the strain axis, indicating that the axial stiffness of the steel bar decreases with the increase in tensile stress, but the stiffness of SCAHRB400 steel bars

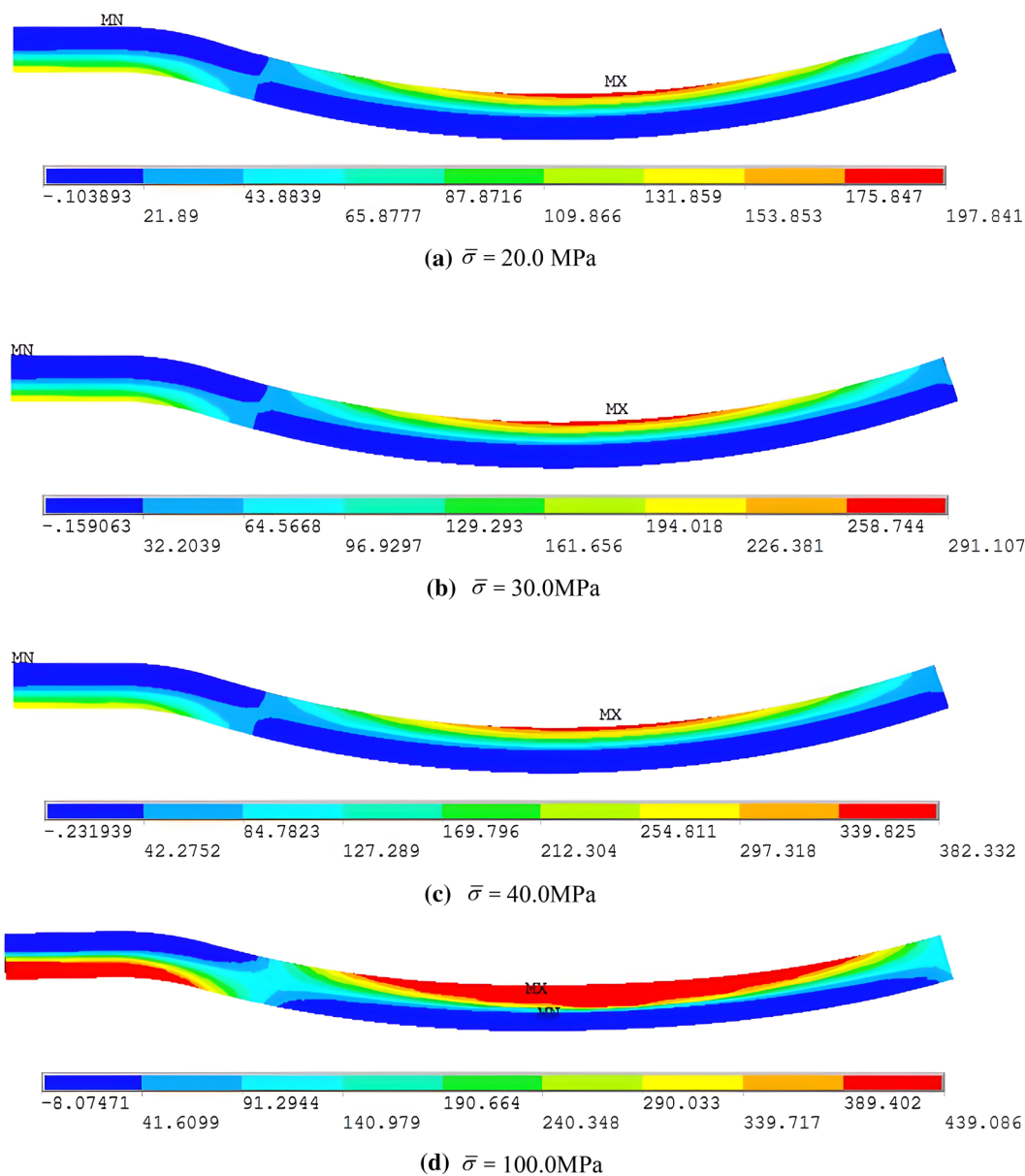


Fig. 14 σ_x stress cloud of specimen 36S (unit: MPa)

is always greater than that of the slightly curved arc HRB335 steel bar. Under the same stress, the strain of slightly curved arc HRB335 steel bars is greater, so the stress of the steel bar across a wide slot caused by concrete expansion or contraction in construction may be smaller.

4 Conclusions

The arc segment of the new type of SCAHRB400 steel bars can be adapt to the temperature deformation of concrete and solve the problem of temperature-induced

stress loss without cutting the steel bars in mass concrete. In this article, tensile tests were carried out on five types of SCAHRB400 steel bars. Considering geometric and material nonlinearities, the numerical simulation on the tensile properties were also investigated. From the tensile and numerical simulation results, the following conclusions can be drawn.

(1) SCAHRB400 steel bars are prone to local yielding near the crown of large arches and at the connection of horizontal and arc sections. The average stress level of local yield of each SCAHRB400 steel bar varies and is not

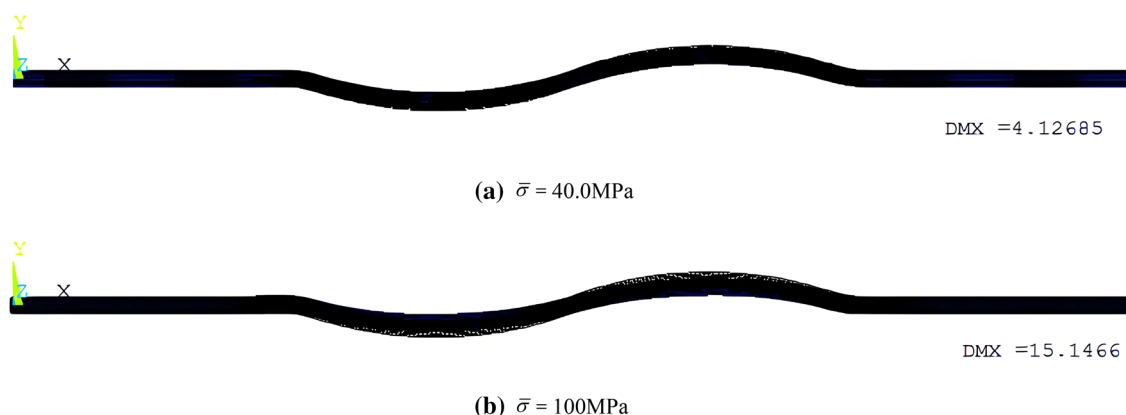


Fig. 15 Deformation diagram of specimen 36S (unit: mm)

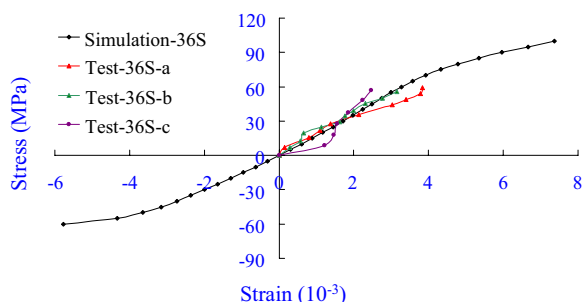


Fig. 16 Comparison of test and numerical simulation equivalent stress–strain curves of specimens 36S

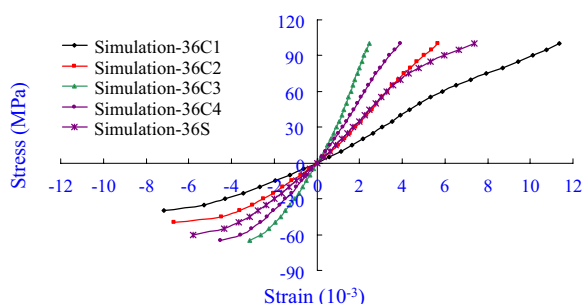


Fig. 17 Numerical equivalent stress–strain curves of specimens 36C1–36C4 and 36S

less than 40 MPa. The equivalent stress–strain curves of SCAHRB400 steel bar specimens are not only related to the vector span height, but also related to the shape of the arc.

(2) The numerical simulation equivalent stress–strain curves have good regularity. When the SCAHRB400 steel bar is compressed, the equivalent stress–strain curve

is concave toward the strain axis, and the axial stiffness of the steel bar decreases as the compressive stress increases. When the SCAHRB400 steel bar is in tension, there is a turning point in the equivalent stress–strain curve, and the curve is concave toward the stress axis, that is, with the tensile stress increases the axial stiffness of the steel bar increases. At this time, the steel bar is straightened, the decrease in vector span height caused by the increase in stiffness is greater than the decrease in stiffness caused by the increase in the plastic zone of the steel bar. Then, the curve is concave toward the strain axis, that is, with the tensile stress increases the axial stiffness of the steel bar decreases. The average stress level at the turning point of different types of SCAHRB400 steel bars varies. The higher the vector span height is, the lower the stress level is, no less than 50 MPa.

(3) The differences in size of the three specimens of each type of the slight curved arc steel bars, the small stiffness of the slight curved arc steel bars in initial tension, the displacements are not easy to measure accurately, thus the equivalent stress–strain curves obtained from the three specimen tests of each type of the slight curved arc steel bars are somewhat different, but they are all in the vicinity of the numerical simulation curves. The test values and numerical simulation values are not very different, indicating that the numerical simulation curves are reliable.

(4) The equivalent stress–strain curves of slightly curved arc HRB400 and HRB335 steel bars have the similar changing law. When the stress is small, the tensile stiffness and compressive axial stiffness of them are similar; when the stress is larger, the axial stiffness of slight curved arc HRB400 steel bars is greater than that of slight curved arc HRB335 steel bars.

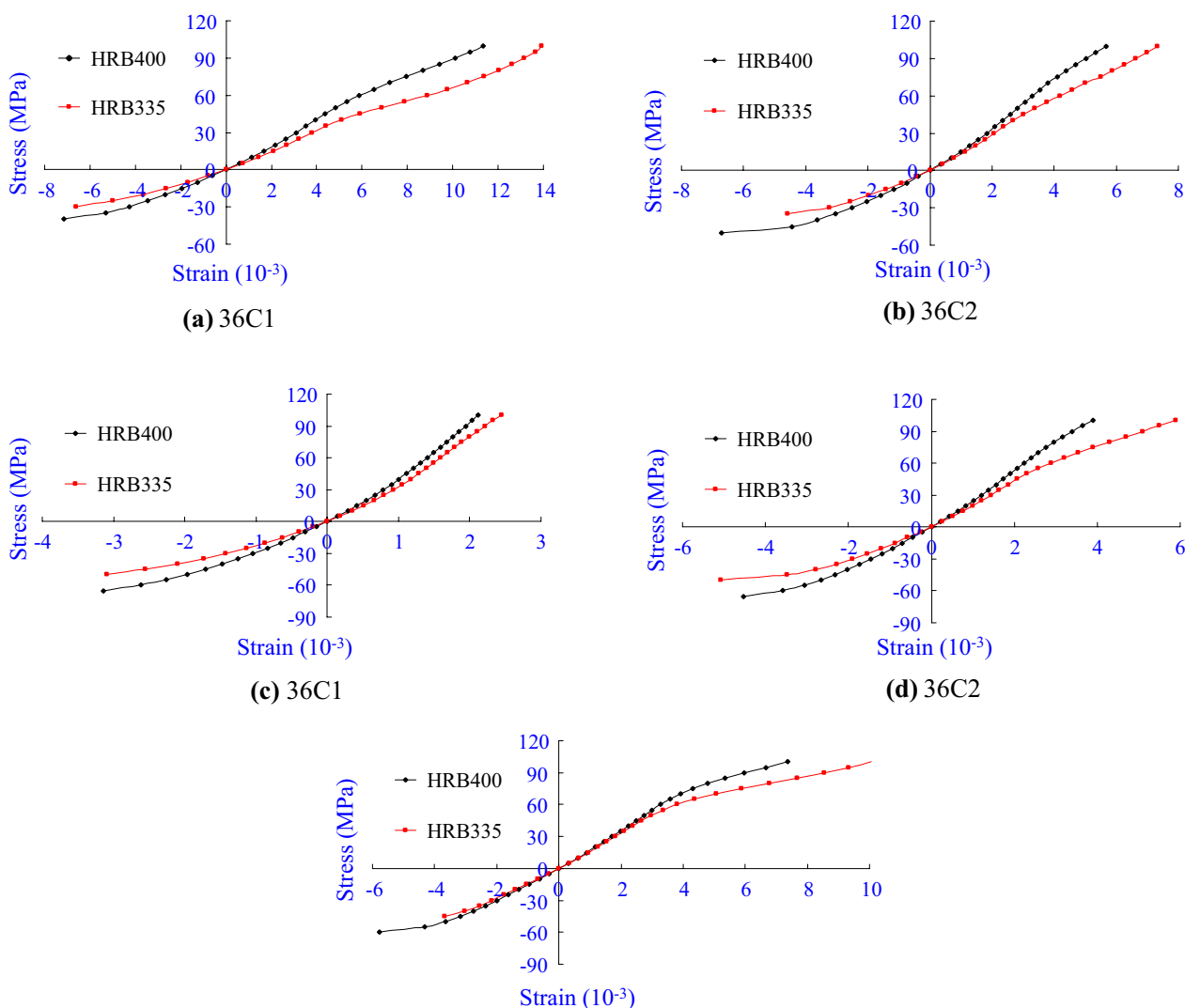


Fig. 18 Comparison of equivalent stress–strain curves of HRB400 and HRB335 steel bars

Acknowledgements

This research has been supported by China Scholarship Council; the Natural Science Research Project of Jiangsu Province Colleges and Universities (21KJD560002), China; Suqian Natural Science Foundation Project (K202012), China; Project funded by the research and innovation team of engineering structure seismic technology of Suqian University in 2020, China; Suqian City Guiding Science and Technology Plan Project (Z2020137), China; Research and Innovation Team Project of Suqian College (2021TD04), China; and the Fifth Provincial Research Funding Project of "333 High-level Talent Training" in 2020 (BRA2020241), China.

Author contributions

CS contributed to conceptualization, funding acquisition, investigation, project administration, resources, and writing. MZ contributed to investigation, supervision, validation, project administration, writing—review and editing. ZW and BC was involved in in formal analysis and methodology. LG and QY contributed to funding acquisition, investigation. HZ and WZ was involved in in formal analysis and methodology, project administration. JY was contributed to investigation and funding acquisition. All the authors read and approved the final manuscript.

Authors' information

Li Gao is a lecturer of School of Civil Engineering and Architecture at Suqian College.
 Mei-Ling Zhuang is an Associate Professor of School of Transportation and Civil Engineering at Nantong University.
 Fangzhi Zhu is a Professor of School of Civil Engineering and Architecture at Suqian College.
 Chuanzhi Sun is an Associate Professor of School of Civil Engineering and Architecture at Suqian College.
 Jun Yang is a lecturer of School of Civil Engineering at Suzhou University.

Availability of data and materials

The data and materials used to support the findings of this study are available from the corresponding author upon request.

Declarations

Ethics approval and consent to participate

Not applicable.

Consent for publication

All the authors agree that the article will be published after acceptance.

Informed consent

Informed consent was obtained from all individual participants included in this study.

Competing interests

The authors declare that they have no competing interests.

Author details

¹School of Civil Engineering and Architecture, Suqian College, Suqian 223800, China. ²Jiangsu Province Engineering Research Center of Prefabricated Building and Intelligent Construction, Suqian College, Suqian 223800, China. ³School of Transportation and Civil Engineering, Nantong University, Nantong 226019, China. ⁴School of Civil, Environmental & Mining Engineering, The University of Adelaide, Adelaide 5005, Australia. ⁵School of Civil Engineering, Suzhou University of Science and Technology, Suzhou 215129, China.

Received: 7 November 2022 Accepted: 22 March 2023

Published online: 03 July 2023

References

- Chen, P. P., & Zhang, G. (2014). Study on the prevention measures and causes of cracks in arch crests of galleries in high concrete dams. *Advanced Materials Research*, 3149, 919–921.
- Gao, F. L., & Fang, Y. W. (2013). Temperature cracks controlling technology for the mass concrete in solid sections of lower pylon column. *Applied Mechanics and Materials*, 467, 262–269.
- Jiang, X. P., Wang, S. L., Duan, S. X., & Sun, Y. (2007). Analysis of the mechanism of temperature cracks in super-volume concrete and new countermeasures for crack control. *Concrete*, 12, 98–102.
- Li, S. H., Wang, Z. Y., Yang, L. Y., Deng, X. M., Li, Y. (2017). Study on the causes and prevention measures of cracks in high crushed concrete dams. *Water Resources and Hydropower Technology*, 48(1), 98–102.
- Liu, X. H., Zhou, C. B., Chang, X. L., Zhou, W. (2010). Simulation of temperature crack expansion process in mass concrete. *Geotechnics*, 31(8), 2665–2676.
- Lu, X. C., Chen, B. F., Tian, B., Li, Y., Lv, C., & Xiong, B. (2021). A new method for hydraulic mass concrete temperature control: Design and experiment. *Construction and Building Materials*, 302, 124167.
- Ma Y. Z. Study on the contact state of reinforcement and transverse joints in the bottom slab of the upper gatehead of Tingzikou. Master's Thesis, Hohai University, Nanjing, China, 2014.
- Shi, W., & Hou, J. P. (2013). Temperature control performance of bulk concrete with phase change temperature control under different conditions. *Journal of Construction Materials*, 16(6), 1063–1066.
- Woo, H. M., Kim, C. Y., & Yeon, J. H. (2018). Heat of hydration and mechanical properties of mass concrete with high-volume GGBFS replacements. *Journal of Thermal Analysis and Calorimetry*, 132(1), 599–609.
- Xin, J. D., Liu, Y., Zhang, G. X., Wang, Z., Yang, N., Qiao, Y., & Wang, J. (2021). Comparison of thermal cracking potential evaluation criteria for mass concrete structures. *Materials and Structures*, 54(6), 243.1–243.15.
- Yan, L., Wen, Y. D., & Bo, W. (2013). The finite element analysis of temperature cracking propagation process of pouring mass concrete. *Applied Mechanics and Materials*, 302, 499–501.
- Yang, B. G., He, P., Peng, G. Y., & Lu, T. (2019). Temperature-stress coupling mechanism analysis of one-time pouring mass concrete. *Thermal Science*, 23, 231–231.

Publisher's Note

Springer Nature remains neutral with regard to jurisdictional claims in published maps and institutional affiliations.

Submit your manuscript to a SpringerOpen® journal and benefit from:

- Convenient online submission
- Rigorous peer review
- Open access: articles freely available online
- High visibility within the field
- Retaining the copyright to your article

Submit your next manuscript at ► [springeropen.com](https://www.springeropen.com)